Incorporation of time-dependent thermodynamic models and radiation propagation models into IR 3-D synthetic image generation models

J.R. Schott, R. Raqueno, C. Salvaggio, E.J. Kraus

Center for Imaging Science, Digital Imaging and Remote Sensing Laboratory (DIRS)
Rochester Institute of Technology
Chester F. Carlson Building, Rochester, NY 14623-0887

ABSTRACT

A model is presented for generation of synthetic images representing what an airborne or satellite thermal infrared imaging sensor would record. The scene and the atmosphere are modeled spectrally with final bandwidth determined by integration over the spectral bandwidth of the sensor (the model will function from 0.25 - 20 μm). The scene is created using a computer aided design package to create objects, assign attributes to facets, and assemble the scene. Object temperatures are computed using a thermodynamic model incorporating 24 hours worth of meteorological history, as well as pixel specific solar load (*i.e.* self-shadowing is fully supported). The radiance reaching the sensor is computed using a ray tracer and atmospheric propagation models that vary with wavelength and slant range. Objects can be modeled as specular or diffuse with emissivities (reflectivities) dependent on look angle and wavelength. The resulting images mimic the phenomenology commonly observed by high resolution thermal infrared sensors to a point where the model can be used as a research tool to evaluate the limitations in our understanding of the thermal infrared imaging process.

1. THERMAL INFRARED SYNTHETIC IMAGE GENERATION

Thermal infrared (TIR) imagery generated by midwave (3-5 μm) and longwave (8-14 μm) sensors is being increasingly used for a variety of remote sensing applications. Some of this interest is motivated by the temperature information which is encoded in these images while other interest is driven by the need for high resolution sensors with day and night capability. Whatever the motivation, the fact that the appearance of these images is controlled in part by temperature introduces a complex new variable into the image analysis process. As a result, the interpretation of these images becomes very complex, particularly if quantitative information is desired. The appearance of this imagery is a result of the complex interaction of atmospheric effects, local meteorological conditions, solar load, object temperature, object emissivity, look angle, sensor location, and sensor spectral characteristics. The temperature of an object in a scene is a complex function of its thermodynamic properties and the environment in which it is located. The end result is images that exhibit contrast reversals as a function of look angle and time of day and a myriad of other unusual phenomena that even a trained image analyst may find inexplicable.

Thermal infrared synthetic image generation (TIRSIG) offers one potential tool for dealing with this process. If the models used in the TIRSIG process are based as much as possible on first principles physical models, then the images can be analyzed in both the forward fashion to see what effect a phenomena will have on an image and in a reverse fashion to determine what caused an observed effect. This paper describes a TIRSIG model that was developed as an attempt to simulate the complex interactions taking place in the thermal infrared imaging process. It incorporates the results of research on modeling many aspects of the imaging and thermodynamic process. Its overall objective is to determine if phenomena observed in TIR images can be modeled adequately so commonly observed effects can be simulated and the modeling process then used to better analyze the image formation and image analysis process.

From a scientific standpoint, a major value of synthetic image generation is that it can provide a complete end-to-end model of the image chain. The extent to which a modeled scene matches an actual

0-8194-0668-6/91/$4.00

scene provides a measure of how well we understand the imaging process. Conversely, the mismatch between a modeled and an actual scene can provide clues to where our understanding of the physical or engineering principles are flawed.

This effort was aimed at building an improved thermal infrared synthetic image generation model based on physical principles. This new model draws on earlier work which incorporated three-dimensional wire frames, angular emissivity effects, and extensive radiation propagation models for generation of longwave infrared (LWIR) synthetic images. The improved Digital Imaging and Remote Sensing (DIRS) laboratory Image Generation (DIRSIG) model incorporates the following improvements; 1) solar radiometry effects so that midwave infrared (MWIR) can be modeled, 2) a thermal model so that the temperature of each scene element is computed as part of the modeling process, 3) an enhanced ray tracer that generates a full shadow history allowing for proper computation of thermal loads, 4) an enhanced radiometry model that generates and utilizes spectrally dependent variables and finally, 5) an integrated computing environment. These improvements enable the DIRSIG model to simulate many more of the complex physical phenomena that affect TIR images. In particular, solar shadows, specular and diffuse objects, sky and object background effects and the wavelength dependent interplay of the source, sensor, and atmosphere are included. In addition, the thermal model allows for inclusion of thermodynamic variables such as density, heat capacity and absorptivity for each object facet, as well as scene dependent treatment of environmental variables such as wind speed, relative humidity, and air temperature as a function of time. The resultant images clearly reflect these improvements by visually mimicking the phenomenology observed in actual TIR images. No quantitative evaluation of the overall model has yet been performed, however, the effects shown in the simulated images have been observed in actual imagery. In addition, most elements of the overall model have been evaluated and indicate that the model should have reasonable quantitative capabilities.

2. BACKGROUND

Many existent TIR scene generation models are considered corporate confidential or have classified components. As a result the literature is often limited to general descriptions making it difficult to evaluate the true capabilities of these approaches. These same limitations often make it difficult to incorporate components of these models into next generation models. Within these constraints DCS Corporation and Schott (1987)[1] conducted an extensive literature review of models related to TIRSIG which included; CAD/CAM, IR radiation propagation, thermodynamic, energy matter interaction, ray tracing and IR sensor models. They described over 30 models, which include numerous submodels. In many cases these models only perform some part of the overall TIRSIG process or are very specific to a particular set of targets or sensors. Thus only a few comprehensive models exist or can be created by stringing these submodels together.

This review pointed out the capabilities of some existent models in an effort to highlight the features which would be desirable in improved models. Several limitations were noted. First, most of the models are not spectrally dependent (*i.e.* the solution is not done wavelength-by-wavelength for all dependent variables). Second, many of the thermal models do not incorporate the thermal history of an individual pixel in terms of temporal environmental variables such as sun/shadow history, air temperature, wind speed, etc. Third, most of the models do not include emissivity values that are a function of view angle. Fourth, most of the models do not include a capability to deal with specular reflections to a sky or background whose radiance varies with angle. Finally, many of the models are not based on fundamental physical principals making them difficult to validate, integrate or update. With this context in mind, the authors have been working with and evolving certain TIRSIG tools for several years aimed at filling gaps in the modeling process.

The DIRS laboratory at RIT's Center for Imaging Science has had a long term interest in absolute radiometric calibration of TIR imagery with a special interest in correction for atmospheric effects (*cf.*

Schott and Schimminger, 1981[2]; Schott and Volchok, 1985[3]; and Byrnes and Schott, 1986[4]). This interest in quantitative measurements led to the development of methods and devices for measurement of TIR normal and angular hemispheric emissivity values. These bandpass values were then used to estimate the effect of emissivity variation on imaging sensors as described by Schott (1986)[5]. The synthetic scenes used at this time were simple 2-D silhouettes with temperature values assigned to each segment. Bandpass values of atmospheric transmission and upwelled and downwelled atmospheric radiance were also included in these models. While the SIG process used in these studies was primitive, it clearly demonstrated the need for inclusion of angular emissivity effects in TIRSIG. This work was extended by Schwartz *et al.* (1985)[6] to include the effects of specular reflection of background surfaces and downwelled sky radiance. These scenes were still very "flat" with each scene segment treated the same. This effect was addressed by Schott and Salvaggio (1989)[7] who describe incorporating brightness variations within segments by taking texture from images of laboratory physical models or from actual TIRSIG images. This was the first effort to make the TIRSIG images begin to look real. Previous work had been concentrated largely on using SIG to help visualize target-to-background signature assessments and to help to "visually" evaluate the importance of various quantitative improvements to the radiation propagation models. As part of these initial efforts to improve the "realism" of the SIG images, Schott and Salvaggio (1987)[8] used a sensor response model incorporating image degradation using asymmetric two-dimensional convolution kernels to simulate atmospheric and optical detector sampling and scanning effects on the modulation transfer function of the imaging sensor. In addition, an ability to add random and periodic detector noise was developed and implemented. As the scenes became increasingly "real," the interest in simulation and its applications expanded. A full three-dimensional scene generation capability was needed to permit visualization of more diverse and complex scenes. This was achieved by incorporation of CAD/CAM three-dimensional wire frame models and a ray tracer as reported by Warnick *et al.* (1990)[9]. In parallel with these improvements, a series of small scale validation efforts kept pace with the advances in SIG modeling, radiation propagation modeling, and materials measurement. The emissivity modeling was extended by Schott *et al.* (1990)[10] to field measurements and to encompass the 3-5 μm, as well as the 8-14 μm region with improved accuracies. Improved methods for measurement of spectral bidirectional reflectance distribution functions (BRDF) in the visible and SWIR region were demonstrated by Feng (1990)[11] as interest grew in extending SIG to shorter wavelengths to simulate multispectral sensors. Salvaggio and Schott (1989)[12] performed a validation study of the surface-leaving radiance portion of the model, validating the treatment of angular emissivity effects and the background and sky radiance equations used in the models. Shor *et al.* (1990)[13] performed a preliminary validation of the radiometry and ray tracing scheme used in conjunction with the 3-D wire frame modeling.

These studies affirmed the basic quantitative integrity of the methodology used but suggested the need for a variety of improvements. One of the most critical needs was for the incorporation of a thermal model so that temperatures could be predicted for each scene element, facet, or pixel based on object parameters and scene conditions. A second major improvement called for the inclusion of solar reflection effects. The modeling described above had been restricted to the LWIR bandpass where solar reflection and scattering effects are vanishingly small compared to self-emission. In the midwave region and at shorter wavelengths, solar reflection becomes very important and must be included in the SIG process. Spector *et al.* (1991)[14] performed a study which included validation of a thermodynamic model which could be used in the SIG process and which appeared to be quite accurate for passive objects. Salvaggio *et al.* (1991)[15] completed a study which was aimed at generation of spectral atmospheric radiation propagation and energy matter interaction terms needed for modeling solar and thermal radiometric effects associated with horizontal surfaces. This model could be modified for use in the SIG process and could also potentially be used spectrally (*i.e.* on a wavelength-by-wavelength basis) to improve the quantitative accuracy of the process. This is particularly important in wavelength regions where the source, sensor or atmospheric spectral response is not

spectrally flat such as in the MWIR or near the ozone absorption line in the LWIR.

Based on the assessment of the state of the art as described above and the status of the work of the DIRS laboratory at RIT, it was decided to assemble an IR SIG capability with all the base line capability for end-to-end image generation. This model would take advantage of existing approaches and software whenever practical and would emphasize the generation of quantitatively correct radiometric scenes. The objectives of the model were as follows, it should:

1. function in the MWIR and LWIR regions,
2. emphasize radiometry - in terms of dealing with as much radiometric phenomenology as necessary to produce observed phenomena,
3. be capable of dealing with scene elements which would be observed by high resolution airborne systems,
4. use first principles physical models as much as possible, and
5. use simple target and sensor models in the initial versions to permit greater emphasis on the phenomenology.

3. SCENE GENERATION APPROACH

The DIRSIG model is comprised of several submodels. Each of the submodels is described in terms of its functionality and its primary interconnections with other submodels. This treatment is intended to provide the reader with an end-to-end view of the process. Since most of the submodels used are treated in detail elsewhere, only the interconnections are covered here along with the radiometry equations that govern the DIRSIG process and those attributes of the ray tracer that provide the submodel interconnections.

The first part of most SIG processes is the scene geometry submodel which allows creation and location of objects in the scene. The DIRSIG scene geometry submodel uses a commercially available CAD package called AutoCAD (AutoCAD Reference Manual, 1989)[16]. This front end allows the user to interactively build wire frame representations of objects. The DIRSIG scene geometry submodel also allows for the scaling and orientation of objects to form the scene. In addition to forming the structure of objects and backgrounds, it is also necessary to assign material parameters

to each surface in the scene. The DIRSIG scene geometry submodel uses facetized elements each of which has assigned to it attributes which allow all necessary optical and thermodynamic properties of the facet to be accessed. As part of the scene geometry submodel, the geometry data is translated from AutoCAD and formatted into real-world coordinates suitable for input to the DIRSIG ray tracer submodel. This translation and formatting process computes the normal vector outward, the slope, and the azimuthal angle for each facet.

The output from the scene geometry submodel is a hierarchical tree-type data structure which contains facet location, facet geometry, and material attributes and serves as input to the ray tracer submodel. The ray tracer submodel draws on and interconnects all the other submodels to build the final scene. In order to initiate building a scene, the sensor model must be accessed to obtain the sensor location, orientation, angular fields-of-view and the number of pixels to produce in the x and y directions for the raw radiance image. A ray is then traced through each pixel center into the scene. The ray tracer uses a search process to determine which object, which part, and eventually which facet is hit. The hierarchical data structure and the use of bounding volumes around objects and parts facilitate the search process. When a ray-facet intersection is located, a series of computations take place to generate inputs to other submodels.

We will first consider the data that are necessary to run the thermal submodel. The facet already

has associated with it slope and azimuth and material properties needed for thermodynamic and solar absorption computations. The material properties associated with each facet include solar absorptivity, broadband thermal emissivity, thickness, internal heat load, heat capacity, thermal conductivity, exposed area , specularity, and emissivity as a function of view angle and wavelength (if available). The major pixel specific unknowns are the current solar load and the solar history of the pixel. These data are acquired by the ray tracer casting out rays from the intersection point on the facet in the direction where the sun was at each point in time (*e.g.* from the time of the image and on 1/2 hour intervals for the previous 24 hours). The ray tracer determines if an object is hit or not and, therefore, if the pixel was sunlit or not as shown in Figure 1. This information is then submitted to the thermal model to compute the temperature of the individual pixel. The sun location information is computed from the time of day, latitude and longitude of the scene, and the day of the year which are part of the overall scene data structure.

The thermal submodel is built around THERM (*cf.* DCS Corporation, 1991)[17], a temperature generation model, which provides most of its functionality. THERM can either use temporal meteorological data or compute estimates of the necessary data using simple environmental models. These meteorological data are combined with pixel specific material data and solar history and input to the thermal submodel which solves the linear differential heat flow equation for the temperature of the pixel. Figure 2 illustrates some of the variables accounted for in the thermal submodel. THERM's relative ease of implementation, coupled with the fact that it is one of the few thermal models of naturally occurring surfaces which has any degree of validation, made it attractive for use as the thermodynamic model.

The temperature of any pixel is a function of the thermodynamic properties of the facet as well as the environmental history to which it has been exposed. THERM was designed to compute the temperature of facets (assuming no lateral conduction) by combining facet specific parameters (heat capacity, thermal conductivity, thickness, solar absorptivity, exposed area, self-generated power, slope and azimuth angles) with time dependent environmental parameters (direct insolation, diffuse insolation, air temperature, wind exposure, cloud type, speed, air pressure, relative humidity, sky precipitation type and rate). Each computation is initiated with an equilibrium solution at some previous point in time and then the current temperature is solved for using a series of forward chaining solutions to the heat flow equations. For objects with high thermal inertia, it was found necessary to initiate the process as much as 24 hours ahead of the actual simulation time. THERM is designed to accept either measured environmental data or to approximate time dependent environmental data from standard forecast data or weather records. Because solar insolation is such a driving factor in temperature computations, THERM was modified for inclusion in DIRSIG. This modification allowed pixel specific computation of temperature by determining whether the pixel was sunlit at the time of interest and what the shadow history of the pixel had been. This data is then used to modify the temporal insolation data on a pixel specific basis. This capability is essential if realistic computations in the vicinity of shadowing objects is required.

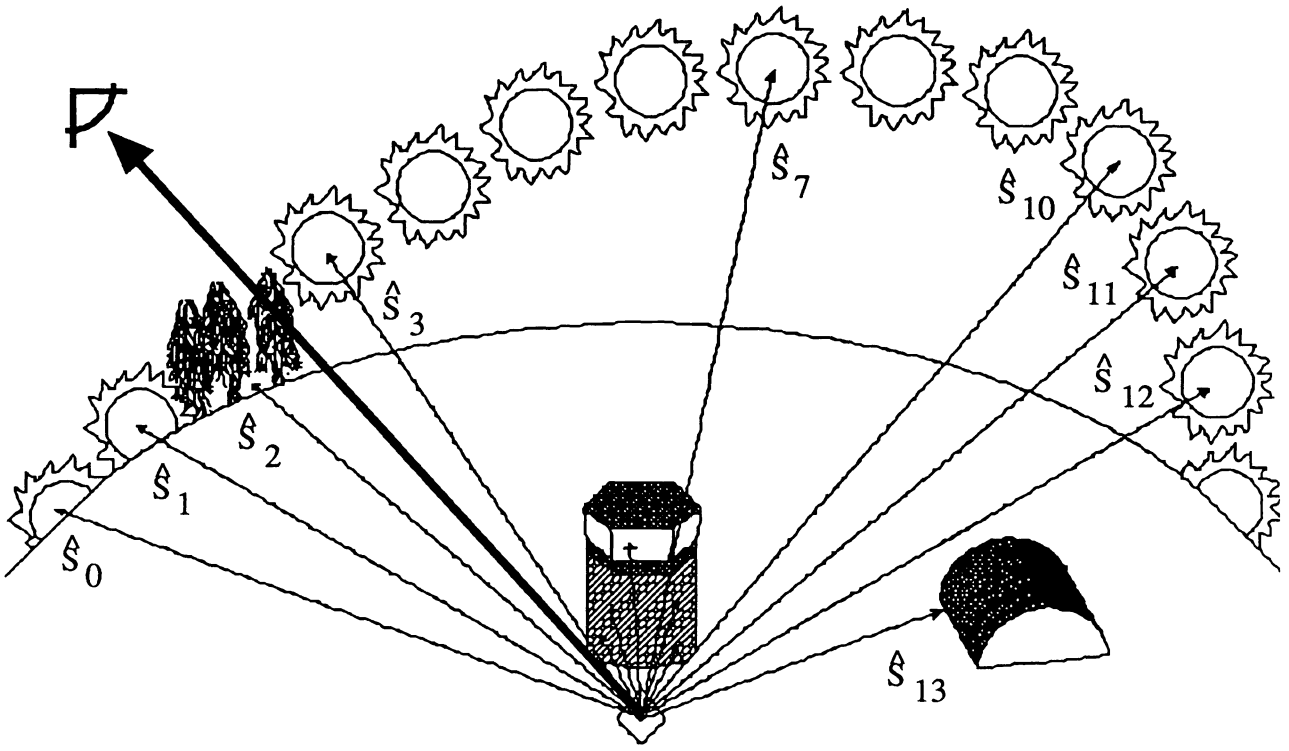

Sun/Shadow History Field

1	1	0	1	0	0	0	1	0	0	1	1	1	0	0	0
0	1	2	3	4	5	6	7	8	9	1 0	1 1	1 2	1 3	1 4	1 5

1 = Sun
0 - Shadow

Figure 1
Illustration of how a ray traced into the scene identifies a pixel center and how rays are cast out from that pixel center to identify sun shadow history

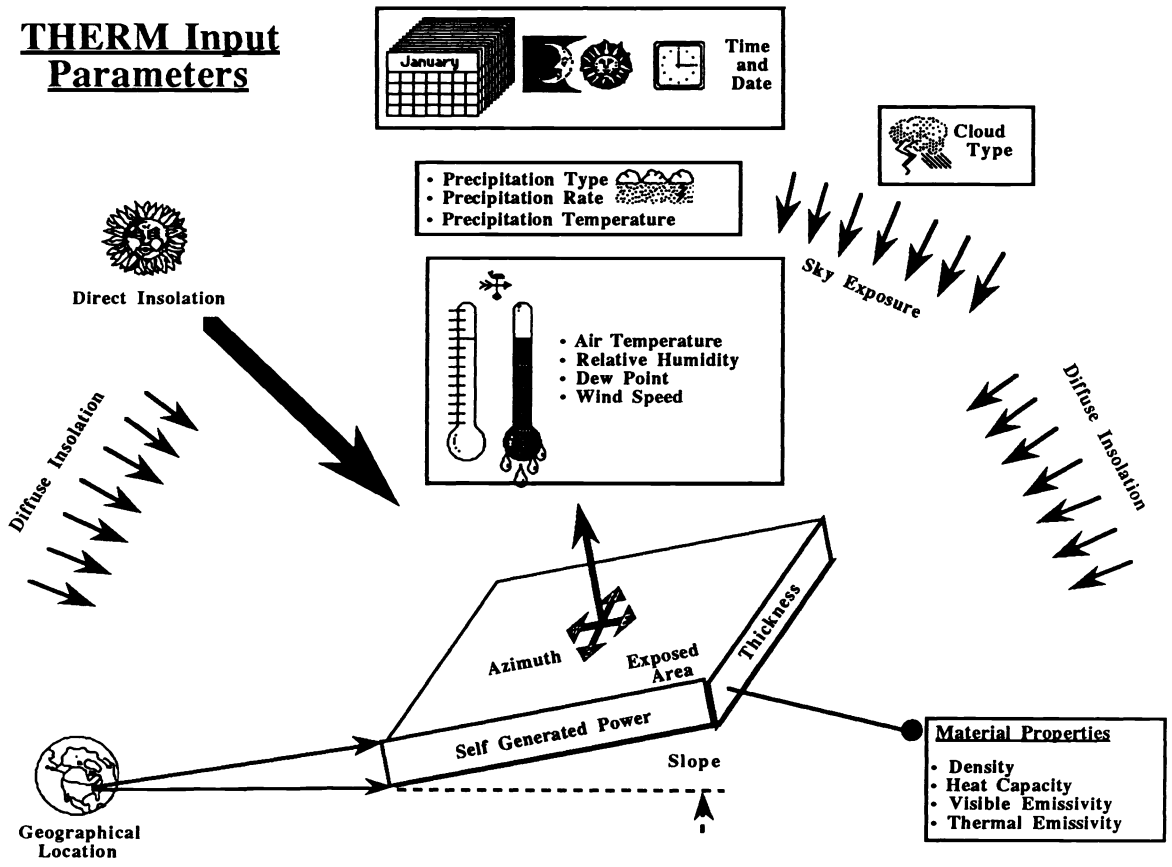

Figure 2
Illustration of some of the variables accounted for by the thermal submodel

Spector *et al.* (1991)[14] have shown THERM to produce accurate temporal predictions of temperatures of passive real world objects. THERM does not compute the conduction between adjacent object facets and therefore does not have all of the functionality of a fully conducting model which would require the use finite element analysis. Such models are complex and require substantial amounts of computing time to add facet-to-facet conduction. THERM does allow for facets with self-generated (internal) power which can, when properly implemented, be used to overcome some of the limitations of non-conduction between facets.

Having received the temperature of the pixel from the thermal submodel, the ray tracer generates additional pixel specific data needed for the radiometry submodel. These include computation of the interaction angles between the incident solar ray and the normal to the facet, the angle between the normal to the facet and the ray from the sensor, the angle between the normal to the earth and the sensor, and computation of the direction of specular reflection if the object is specular. The specular ray is projected to determine whether the sky or a background object is encountered. If a background object is hit, additional data is gathered using the ray tracer and the thermal submodel for the background. If no object is hit, then the radiance from the location in the sky is computed.

The angular data, target temperature, background data, etc. are then passed to the radiometry submodel which computes the radiance reaching the sensor on a wavelength-by- wavelength basis. Figure 3 shows some of the energy paths and energy matter interactions included in the radiometry submodel. The radiometry submodel is built on top of LOWTRAN 7. The atmospheric transmission, upwelled radiance, solar irradiance, and downwelled radiance are precomputed for each wavelength

within the spectral band of interest and for the range of possible slant paths within the scene (*cf.* Figure 4). The appropriate radiometry equation is then solved and numerically integrated over wavelength using the spectral response function of the sensor as a weighing factor to yield the effective integrated radiance at the sensor for each pixel.

Each pixel will fall into one of four categories (*cf.* Figure 3) and will be processed through the appropriate governing equation. For pixels which have diffuse reflectance characteristics (Case 1), the radiance is computed as

$$
\begin{aligned}
L(\theta,\lambda) = \; & \varepsilon(0,\lambda)\, L_T(\lambda)\, \tau_2(\theta_E,\lambda) + \\
& L_T \frac{E_S(\lambda)}{\pi}\, \tau_1(\lambda) \cos(\theta_S)\, (1-\varepsilon(0,\lambda))\, \tau_2(\theta_E,\lambda) + \\
& \left[L_{DE}(\lambda) + L_{DS}(\lambda) \right] (1-\varepsilon(0,\lambda))\, \tau_2(\theta_E,\lambda) + \\
& L_{uE}(\theta_E,\lambda) + L_{uS}(\theta_E,\lambda)
\end{aligned}
\tag{1}
$$

for pixels which have specular reflectance characteristics where the reflected ray bounces to the sky (Case 2), the radiance is

$$
\begin{aligned}
L(\theta,\lambda) = \; & \varepsilon(\theta,\lambda)\, L_T(\lambda)\, \tau_2(\theta_E,\lambda) + \\
& L_T \frac{E_S(\lambda)}{\pi}\, \tau_1(\lambda) \cos(\theta_S)\, (1-\varepsilon(\theta,\lambda))\, \tau_2(\theta_E,\lambda) + \\
& \left[L_{DE}(\theta_{SK},\lambda) + L_{DS}(\theta_{SK},\lambda) \right] (1-\varepsilon(\theta,\lambda))\, \tau_2(\theta_E,\lambda) + \\
& L_{uE}(\theta_E,\lambda) + L_{uS}(\theta_E,\lambda)
\end{aligned}
\tag{2}
$$

for pixels which have specular reflectance characteristics where the reflected ray hits a background object (Case 3), the radiance is computed as

$$
\begin{aligned}
L(\theta,\lambda) = \; & \varepsilon(\theta,\lambda)\, L_T(\lambda)\, \tau_2(\theta_E,\lambda) + \\
& L_T \frac{E_S(\lambda)}{\pi}\, \tau_1(\lambda) \cos(\theta_S)\, (1-\varepsilon(\theta,\lambda))\, \tau_2(\theta_E,\lambda) + \\
& \varepsilon_B(\theta_{BT},\lambda)\, L_{TB}(\lambda)\, (1-\varepsilon(\theta,\lambda))\, \tau_2(\theta_E,\lambda) + \\
& L_B \frac{E_S(\lambda)}{\pi}\, \tau_1(\lambda) \cos(\theta_B)\, (1-\varepsilon_B(\theta_{BT},\lambda))\, (1-\varepsilon(\theta,\lambda))\, \tau_2(\theta_E,\lambda) +
\end{aligned}
$$

$$L_{uE}(q_E,l) + L_{uS}(q_E,l) \tag{3}$$

and for pixels where a ray cast from the sensor heads to the sky (Case 4) the radiance is represented as

$$L(q,l) = L_{DE}(q_{SK},l) + L_{DS}(q_{SK},l) \tag{4}$$

The parameters in Equations 1 through 4 are defined below. It is important to realize that wherever a functional dependence on an angle (*e.g.* q,q_{SK}) is indicated, an array of values are precomputed and the actual value solved by interpolation. All parameters with a functional dependence on wavelength (l) are generated on 100 cm^{-1} intervals over the range 350 - 39850 cm^{-1} (0.25 - 28 mm).

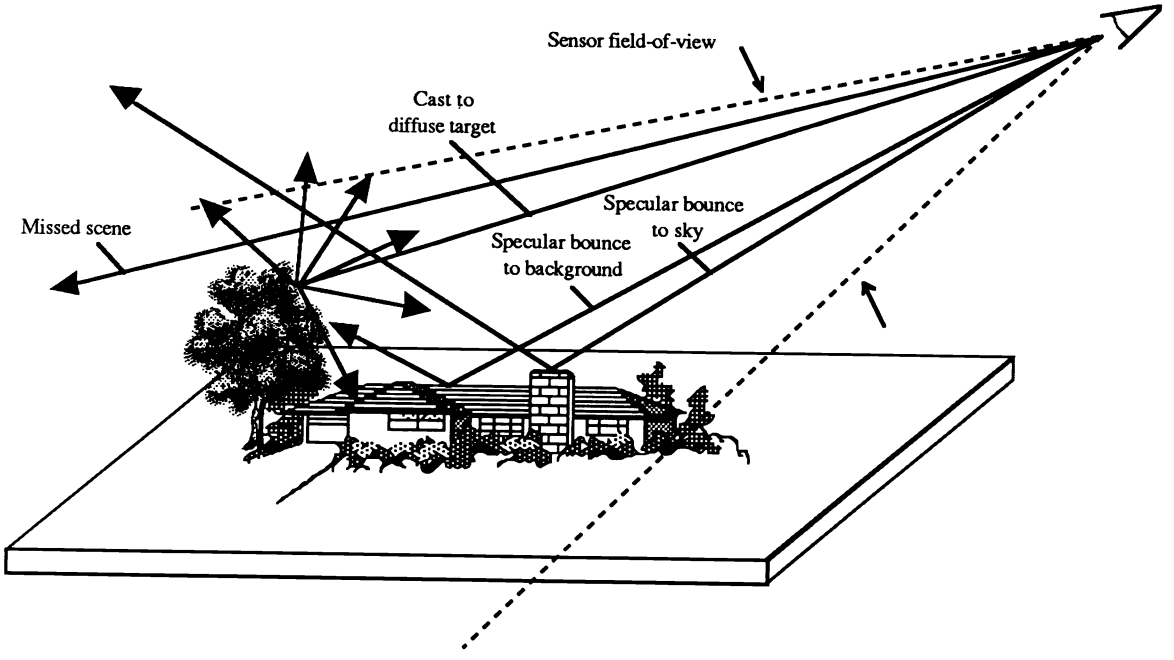

Figure 3
Illustration of the possible ray interactions on a target within the scene

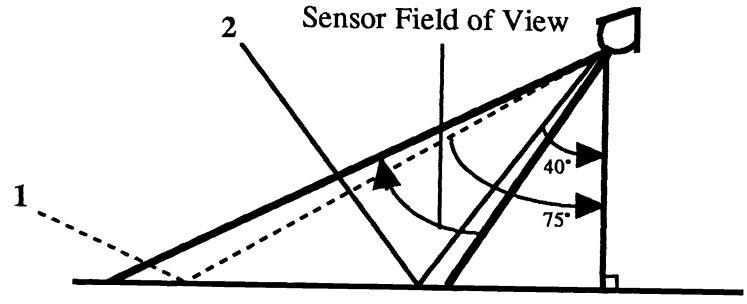

Angle 1 (75°)

Angle 2 (40°)

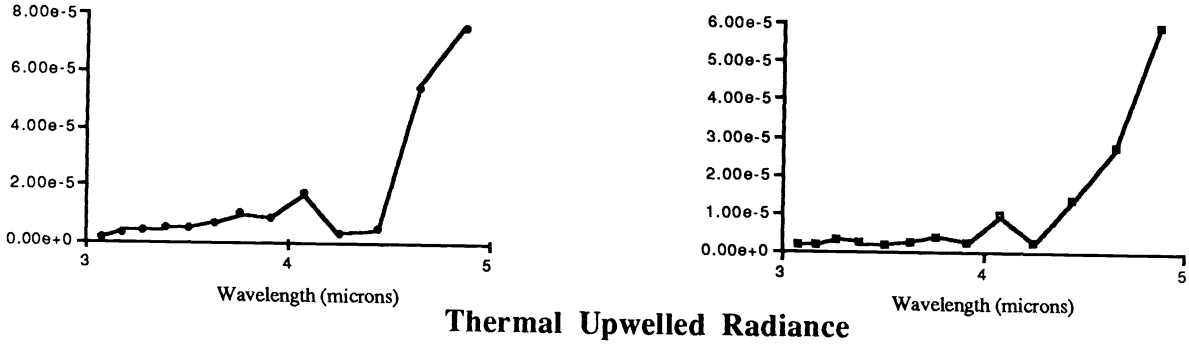

Thermal Upwelled Radiance
TLU

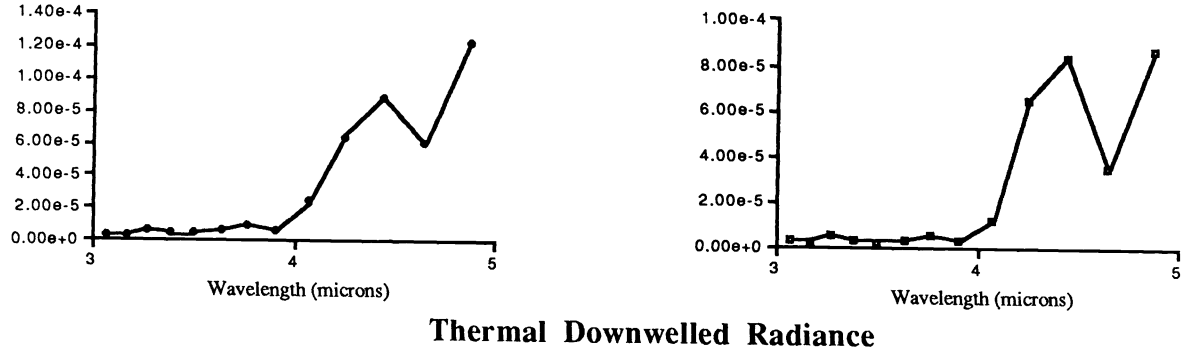

Thermal Downwelled Radiance
TLD

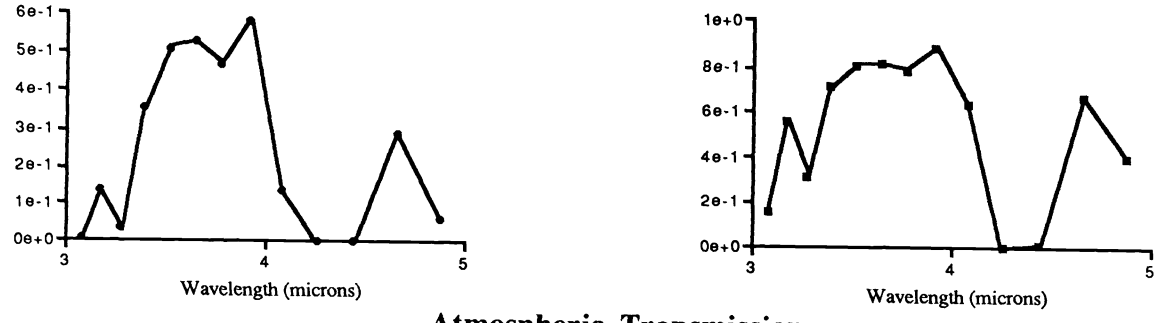

Atmospheric Transmission
TAU 2

Figure 4
Illustration of how radiometric terms vary with both view angle and wavelength

$L(q,l)$	spectral radiance reaching the front end of the sensor
$L_T(l)$	the self-emitted spectral radiance from a blackbody at temperature T (target)
$L_{TB}(l)$	the self-emitted spectral radiance from a blackbody at temperature T (background)
$E_S(l)/p$	the exoatmospheric solar spectral radiance
$L_{DE}(l)$	the downwelled spectral radiance due to self-emission of the atmosphere integrated over the skydome
$L_{DS}(l)$	the downwelled spectral radiance due to scattering integrated over the skydome
$L_{DE}(q_{SK},l)$	the directional downwelled spectral radiance due to self-emission of the atmosphere
$L_{DS}(q_{SK},l)$	the directional downwelled spectral radiance due to scattering
$L_{uE}(q,l)$	the upwelled spectral radiance due to self-emission of the atmosphere along the target-sensor path
$L_{uS}(q,l)$	the upwelled spectral radiance due to scattering along the target-sensor path
$t_1(l)$	the atmospheric spectral transmission along the source-target path
$t_2(q_E,l)$	the atmospheric spectral transmission along the target -sensor path
$e(q,l)$	angular spectral emissivity for the target
$e_B(q,l)$	angular spectral emissivity for the background over the bandpass
q	the angle between the normal to the surface and the sensor-target path
q_S	the angle between the normal to the surface and the sun-target path
q_B	the angle between the normal to the background and the sun-background path
q_E	the angle between normal to the earth at the target and the sensor-target path
q_{SK}	the angle between the normal to the earth and the reflected ray specularly from the sensor at the target
q_{BT}	the angle between the normal to the background and the target hit point
I_T	target sun/shadow flag (1 or 0) (indicates presence of absence of shadow)
I_B	background sun/shadow flag (1 or 0) (indicates presence of absence of

shadow)

The parameters shown above are defined using the preceding submodels and a modified version of LOWTRAN 7 which produces output tables of the standard LOWTRAN radiometric terms as a function of wavelength. Additional terms are generated by manipulation of the basic LOWTRAN code (*e.g.* numerical integration of paths to space to yield downwelled sky radiance). The LOWTRAN derived values can be derived from user supplied atmospheric profile (radiosonde) data or using the standard atmospheres found in LOWTRAN.

After each pixel's radiance has been computed, the composite radiance image can be passed to a sensor model such as described by Schott and Salvaggio (1989)[7]. This model allows for geometric corrections to a radiance image to account for blurring by the atmosphere, optics, sensor motion, and electronics as well as for sampling effects of the detector and electronics. This type of sensor submodel can also add random and periodic noise effects. It is also possible to add random or periodic texture within an object class to simulate variations in optical or thermal properties within the material type. For the images presented here, texture variations and degradations due to the sensor are not included except for radiometric quantization.

4. RESULTS

The results of phenomenological testing of the model are presented here. The intent was to exercise several aspects of the model and determine if phenomena normally observed in midwave infrared and longwave infrared images could be simulated. A major test of the model was to determine how well it would model variations in the appearance of a scene as a function of time. Figure 5 shows eight frames from a 24 hour sequence simulating parked aircraft. The images show the scene from 8 a.m. to 3 p.m. as simulated in the 3-5 mm bandpass.

The effects of the differential thermal mass of the runways, parking apron, grass and aircraft are clearly simulated with high thermal mass objects heating up more slowly and staying warm longer. The shadows move about the scene as expected (note the planes are facing north). In particular, note the separation into a sharp and a blurred shadow cast by the nose of the large aircraft in the early afternoon. In this region of the spectrum, the photon flux from reflected solar photons is of the same order of magnitude as from self-emitted (thermal) photons. The sharp shadow is formed when the sun is blocked. The blurred shadow is caused because the region to the west of the current shadow was previously in shadow and is therefore cooler and radiating fewer photons. A similar image sequence in the 8-14 mm region shows only the thermal shadow. Again this is an expected result since very few solar photons are observed to 8-14 mm window.

The variation in brightness across the surface of the hanger and the aircraft fuselage also simulate observed phenomena caused by differential heating due to the angle between the surface normal and the sun in addition to variations in emissivity associated with differences between the surface normal and view angle.

The DIRSIG models capability for simulating weather conditions on thermal infrared images is shown in Figure 6. This sequence of images illustrates the effect of various wind flow conditions. These images simulate how wind speed has a significant impact on reducing the contrast in thermal images. The images are simulated as though the wind had blown at a constant speed of 0, 10, 20, or 30 mph for the 24 hours preceding the time of image simulation. This shows a well known phenomena of contrast reduction associated with wind speed and the non-linearity of this process (*i.e.* rapid contrast reduction and then only more gradual contrast reduction at higher wind speeds). The effects of the atmosphere and view angle variations are illustrated in Figure 7. These images represent a series of acquisitions at a fixed range of 10 km at a series of view angles in the 8-14 mm bandpass.

effects of the atmosphere and view angle variations are illustrated in Figure 7. These images represent a series of acquisitions at a fixed range of 10 km at a series of view angles in the 8-14 μm bandpass. The optical depth at the more grazing angles is much deeper than at near vertical views resulting in reduced contrast with the angle. Also shown in these images is the effect of varying emissivity as a function of view angle. This is most dramatic at the lowest (most grazing) view angle where the top of the hanger becomes very dark (cold). At grazing angles the reflectivity of specular materials (such as the painted metal hanger roof) becomes near mirror-like. This results in a specular glint to a "cold" sky. These synthetic images mimic the phenomena that are observed in actual imagery. In general, the synthetic images generated by the model produce to first order most of the thermal, atmospheric, and optical phenomena observed by the thermal infrared sensors. They do not provide information as to how well the model performs in a quantitative fashion. Many aspects of thesubmodels have of course been quantitatively evaluated. Spector *et al.* (1991)[14] describes a limited evaluation of the thermal model indicating that for passive objects it tracks temperature to better than 1.5K when good meteorological data are available. Several aspects of LOWTRAN's performance have been documented (*cf.* Kneizys *et al.* 1988)[18]. The angular emissivity and surface-leaving radiance components of the model were tested by Salvaggio and Schott, 1989[7] and the link to a ray tracer was further tested by Shor *et al.* 1990[13]. These data indicate that earlier versions of the optical interactions and ray tracer would be expected to yield sensed radiance values within 2.5K of the actual values when the surface temperatures are known. These peripheral tests tend to add credence to the overall model, however, future efforts should address their quantitative accuracy.

5. CONCLUSIONS AND RECOMMENDATIONS

The synthetic image generation model described here exhibits a wide range of capabilities. The model starts with three-dimensional geometric objects with complete sets of physical descriptors, assembles these individual objects into a faceted scene, assigns temperatures to each facet in the objects based on a thermodynamic model, uses ray tracing techniques to determine the radiometric interaction which occurs at each point in the scene, computes the radiance reaching the front-end of a sensing system, models the sensor used to record the signal and produces a realistic synthetic image in the LWIR or MWIR bandpass. The images produced depict most of the phenomena that one would expect to see in real imagery with proper radiometric fidelity and geometric interactions. This tool enables scientists, engineers and analysts to visualize the scenes which may be produced by a sensor of interest under a variety of meteorological and collection geometry conditions. The "what if" research that can be conducted with such a tool and the educational potential for image analysts is nearly unlimited.

While the model appropriately mimics much of thermal imaging phenomena, several weaknesses remain. It's overall quantitative accuracy needs to be tested and the limitations of each of the submodels identified. The thermal model is quite effective in dealing with environmental influences, however, it does not account for internal conduction and lateral dispersion of energy from internal heat sources such as automobile engines. Future efforts should consider using a heat flow model incorporating internal conduction effects or a hybrid model which merges the current model with an internally conducting model. The radiometry model described here is limited in that objects are treated as either completely diffuse or completely specular. The potential for fully incorporating bidirectional reflectance factors (BRDF) should be considered. If this were to be fully implemented, the effects of background objects on both the thermodynamic and radiometric models could be more accurately modeled. This improvement in the accuracy might however be expensive in terms of computing time, therefore, enhancements that don't involve full BRDF but which reduce the current limitations should also be considered. Finally, for uses where spatial variation within a material class is important, improved methods for modeling and incorporating texture into TIRSIG images should be studied.

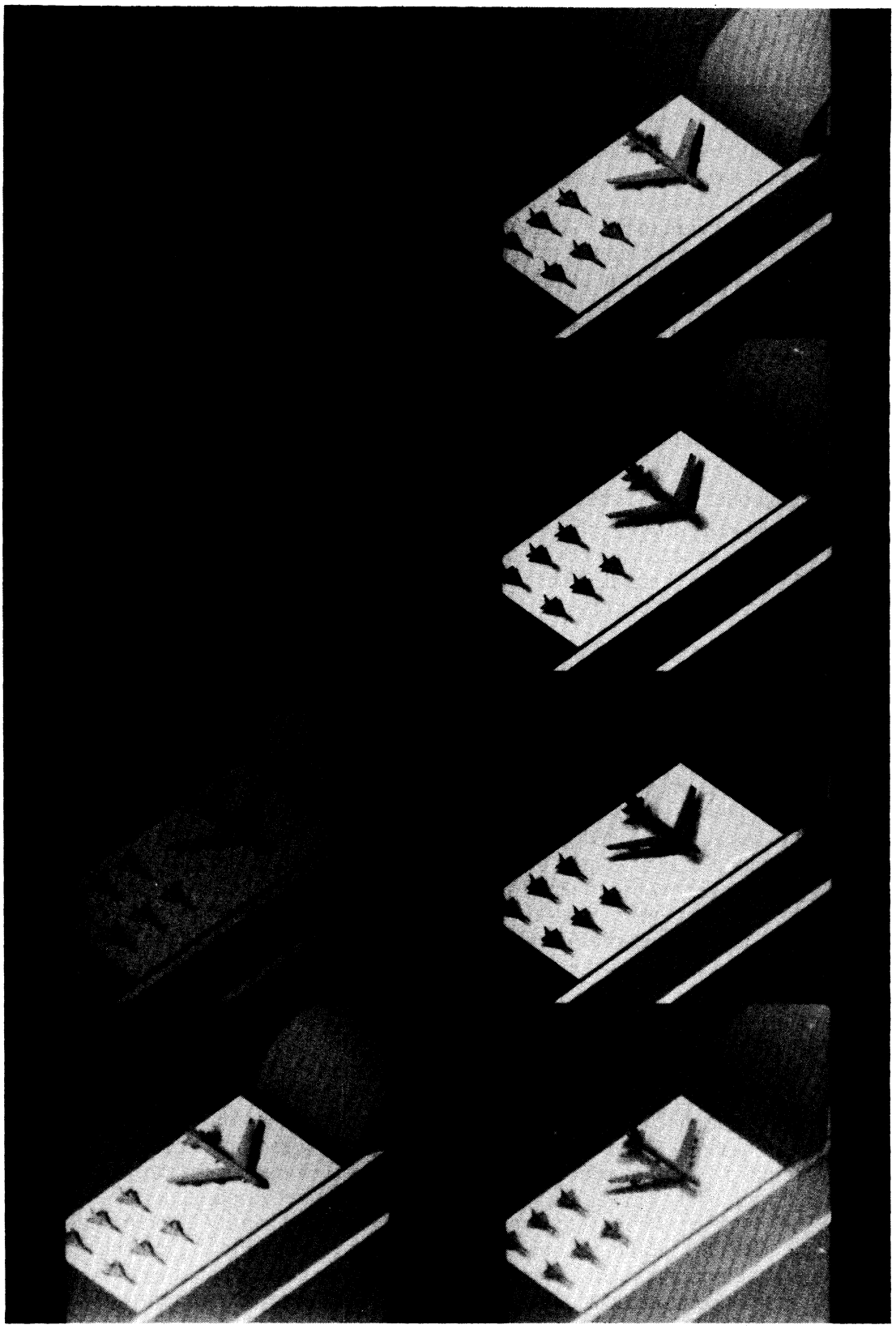

Figure 5

Simulated images in the 3-5 μm bandpass. These images simulate how the scene would appear at 8, 9, 10, and 11 a.m. left column and 12 noon, 1, 2, and 3 p.m. right column.

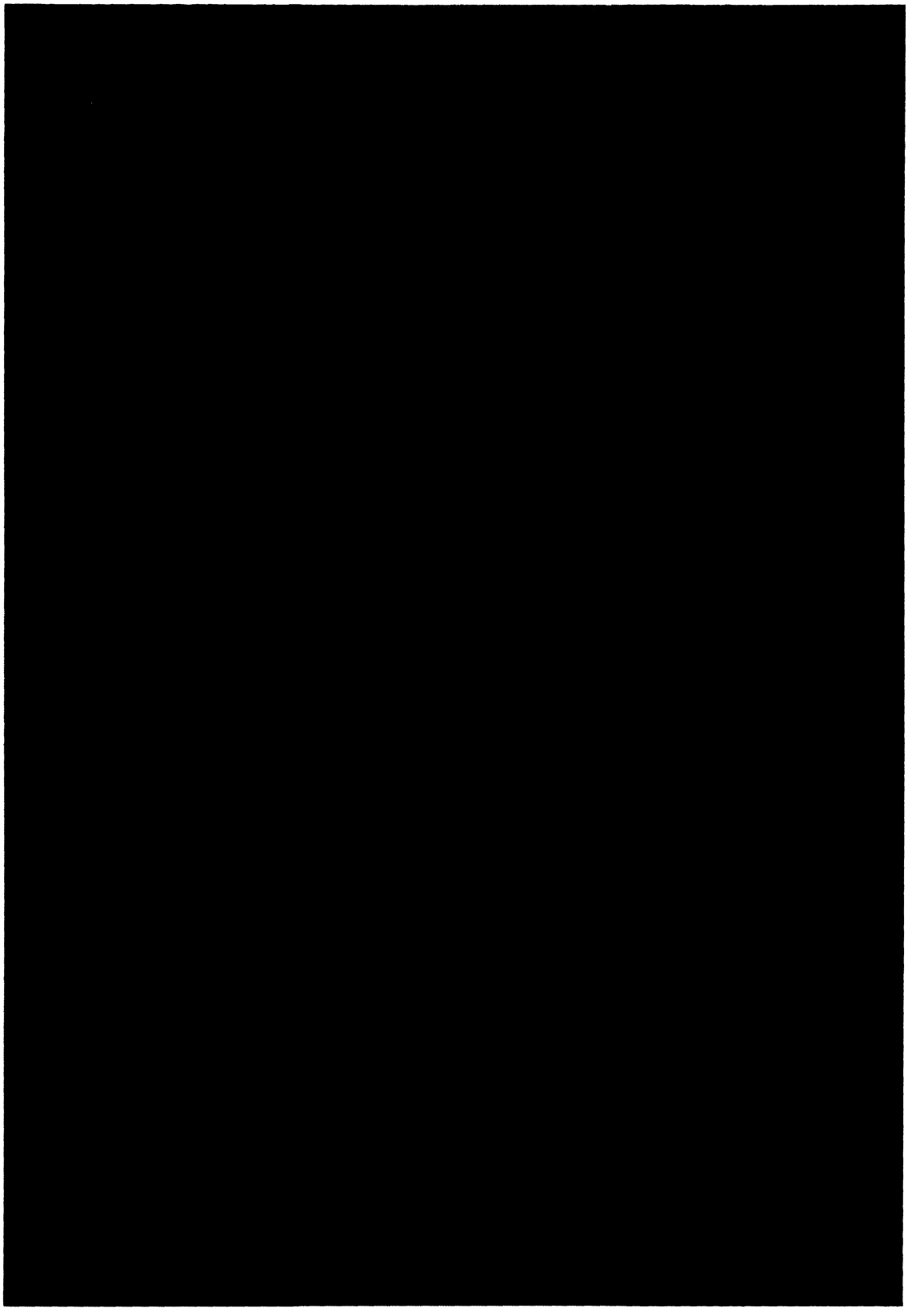

Figure 6

Simulated images in the 8-14 μm bandpass. These images show how the scene would vary if the wind speed changed. They were modeled with fixed wind speeds of 0, 10, 20, and 30 mph (top to bottom) for the previous 24 hours.

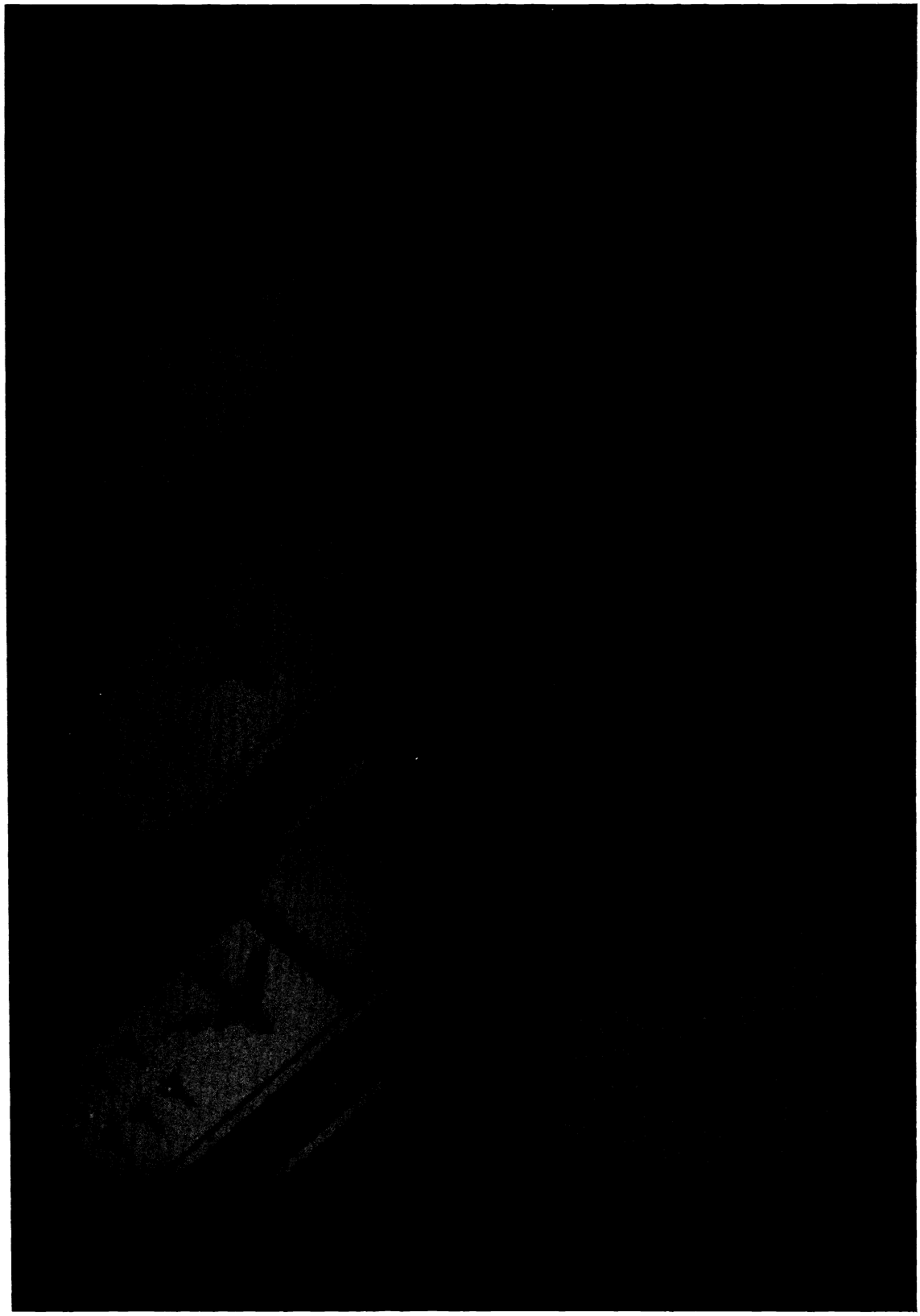

Figure 7

Simulated images in the 8-14 μm bandpass. These images show how the scene would appear when viewed from a fixed slant range at angles from the vertical of 0, 15, 30, 45, 60 and 75°.

6. REFERENCES

1. DCS Corporation and J.R. Schott, "Automatic target recognition/counter-countermeasures technology development program model review," prepared for Autometric Incorporated, DCS Report No. 13430LT003Z, 1987
2. Schott, J.R. and E.W. Schimminger, "Data use investigations for applications explorer mission A (Heat Capacity Mapping Mission)," Calspan Report No. 6175-M-1, NASA Accession #E81-10079, January 1981
3. Schott, J.R. and W.J. Volchok, "Thematic Mapper thermal infrared calibration, Photogrammetric Engineering and Remote Sensing, Vol. 51, No. 9, September 1985
4. Byrnes, A.E. and J.R. Schott, "Correction of thermal imagery for atmospheric effects using aircraft measurement and atmospheric modeling techniques," Applied Optics, Vol. 25, No. 15, August 1986
5. Schott, J.R., "Incorporation of angular emissivity effects in longwave infrared image models," Proceedings of the SPIE Symposium, Infrared Technology XII, Vol. 685, San Diego, CA, August 1986
6. Schwartz, I.B., K.A. Snail, J.R. Schott, "Infrared halo effects around ships," Naval Research Laboratory Memorandum 5529, 1985
7. Schott, J.R. and C. Salvaggio, "LWIR radiometric modeling for use with synthetic scene generation 1987/88 results," Final Report RIT/DIRS 87/88-51-122, prepared for Contract RD-86-6843 (Task 3), Office of Development and Engineering, Central Intelligence Agency, January 1989
8. Schott, J.R. and C. Salvaggio, "Inclusion of sensor noise in radiometric models for generation of synthetic longwave infrared images," Proceedings of the SPIE, Three-Dimensional Imaging and Remote Sensing, San Diego, CA, August 1987
9. Warnick, J.S., E. Shor, J.R. Schott, "Thermal infrared scene simulation," Final Report RIT/DIRS 89/90-51-133, prepared for United States Department of Energy, January 1990
10. Schott, J.R., M. Fairchild, X. Feng, R. Raqueno, B. Brower, T. Gallagher, "Techniques for measurement of the optical properties of materials," Final Report RIT/DIRS 89/90-51-134, prepared for United States Department of Energy, January 1990
11. Feng, X., "Comparison of methods for generation of absolute reflectance factor measurements for BRDF studies," M.S. Thesis, Rochester Institute of Technology, Center for Imaging Science, December 1990
12. Salvaggio, C. and J.R. Schott, "Laboratory techniques for assessment of longwave infrared radiometric models for synthetic scene generation," Proceedings of the SPIE, Infrared Technology XV, Vol. 1157, San Diego, CA, August 1989
13. Shor, E.H., C. Salvaggio, and J.R. Schott, "Three-dimensional longwave infrared (LWIR) synthetic image generation incorporating angular emissivity effects using raytracing techniques," presented at the SPIE 35th Annual International Symposium on Optical & Optoelectronic Applied Science and Engineering, San Diego, CA, August 1990
14. Spector, D.N., P.F. Lambeck, S.L. Sheller, S.C. Sawtell, D.K. Rankin, J.R. Schott, "Air Force infrared simulated image models," Proceedings of the Infrared Information Symposia, Vol. 35 #2, January 1991
15. Salvaggio, C., G. Braun, J.R. Schott, "SVGM a spectral vector generating model using the LOWTRAN 7 and SCATRAN atmospheric propagation codes," RIT/DIRS 90/91-63-141, prepared for Eastman Kodak Company, Federal Systems Division, January 1991
16. AutoCAD Release 10 Reference Manual/Autodesk Inc., 1989
17. DCS Corporation, "AIRSIM thermal signature prediction and analysis tool model assumptions and analytical foundations," DCS Technical Note 9090-002-001, 1991
18. Kneizys, F.X., E.P. Shettle, L.W. Abreu, J.H. Chetwynd, G.P. Anderson, W.O. Gallery, J.E.A. Selby, and S.A. Clough, Users Guide to LOWTRAN 7, AFGL-TR-88-0177, Environmental Research Papers, No. 1010, Air Force Geophysics Laboratory, Optical/Infrared Technology Division, Hanscom AFB, Maryland, August 1988.